





Cite this: DOI: 10.1039/d5nr02432c

A magnetic hybrid sol–gel ionic network catalyst for direct alcohol esterification under solvent-free conditions†

Maryam Faraji,^a Fariborz Mansouri,^{*b} Babak Karimi^{*a,c} and Hojatollah Vali^d

A novel cross-linked organic–inorganic magnetic ionic network nanoparticle (MINN) comprising core–shell silica-coated iron oxide nanoparticles as the seeds and high loading immobilized imidazolium-based poly(ionic liquid) (PIL) linkers was prepared *via* a two-step microemulsion and radical polymerization method. Subsequently, by a simple counter-anion exchange method, the sulfonic acid anion was stabilized on the support to prepare a powerful solid acid catalyst. The material was characterized with various techniques including thermogravimetric analysis (TGA), Fourier transform infrared spectroscopy (FTIR), N₂ adsorption–desorption, CHNS elemental analysis, transmission electron microscopy (TEM) and vibrating sample magnetometry (VSM). Optimization experiments demonstrated that the best results were achieved in the esterification of both primary and secondary alcohols with acetic acid (5–7 equivalents), using as little as 0.1 mol% of the catalyst at 85 °C under solvent-free conditions. Under these optimized conditions, the developed catalyst demonstrated exceptional catalytic activity, selectivity, water resistance, and durability in the direct esterification of primary and secondary benzylic, aliphatic, and cyclic alcohols, yielding the corresponding esters in excellent yields ranging from 78% to 99%. Notably, the catalyst could be recovered and reused for up to 10 cycles without any significant loss in its performance and magnetic susceptibility. The strong reactivity and selectivity of the developed catalyst can be attributed to the well-distributed acidic sites on the 3D PIL support, which offers accessible nano-ionic active sites. Additionally, the hydrophobic nature of the network catalysts facilitates the easy diffusion of starting materials and provides excellent water repellency, thereby enhancing the reaction yield.

Received 7th June 2025,
Accepted 10th July 2025
DOI: 10.1039/d5nr02432c

rsc.li/nanoscale

Introduction

Recently, ionic liquids (ILs) have received much attention due to their outstanding properties such as negligible vapor pressure, high boiling point, chemical and thermal stabilities, non-flammability, good solvating ability, tunable hydrophobicity, high conductivity, vast electrochemical potential, and the ability to adjust acidity. Due to their ability to use a variety of cations and anions in their structure, these compounds have a

wide range of applications in various fields such as separation technologies, synthesis of materials, surface modification technology, sensors, electrochemistry, and analytical chemistry.^{1,2} For instance, the acidity of ILs can be adjusted by the alkyl sulfonic acid or carboxylate acid groups in the side chains of cations or using AlCl₄[−] or HSO₄[−] as anions.³ However, most of the ILs employed are toxic and/or their production is costly; thus, their homogeneous usage exhibits concerns associated with the difficulty in recycling and product purification. More importantly, owing to their high viscosity, regularly, a small amount of IL known as the “diffusion layer” efficiently contributes as the appropriate reaction medium in a chemical process.⁴ To overcome this problem, the concept of supported ionic liquids (SILs) has been developed in which a tunable and lower amount of immobilized IL effectively cooperates in the reaction process while the whole system is easily recyclable.^{5–7} Considering the facile adjustability and functionalization of ILs, SILs are usually prepared by depositing ILs on the surface of solid supports using various methods, including physisorption, condensation, polymerization, covalent bonding, sol–gel, *etc.*⁴ In this route, IL loading

^aDepartment of Chemistry, Institute for Advanced Studies in Basic Sciences (IASBS), Prof. Yousef Sobouti Boulevard, Zanjan 45137-66731, Iran.

E-mail: karimi@iasbs.ac.ir, bkarimi48@gmail.com

^bDepartment of Chemical Technologies, Iranian Research Organization for Science and Technology (IROST), Tehran, Iran. E-mail: f.mansouri@irost.ir

^cResearch Centre for Basic Sciences & Modern Technologies (RBST), Institute for Advanced Studies in Basic Sciences (IASBS), Prof. Yousef Sobouti Boulevard, Zanjan 45137-66731, Iran

^dDepartment of Anatomy, Cell Biology and Facility for Electron Microscopy Research, McGill University, Montreal, Quebec H3A 2A7, Canada

† Electronic supplementary information (ESI) available. See DOI: <https://doi.org/10.1039/d5nr02432c>

is a critical issue because it directly determines the entire performance of the material. Generally, it is possible to immobilize ILs on the surface in two ways: by impregnation on the support and by covalent bonding. In the impregnation method, the amount of IL loading is large but leaching usually occurs during the reaction owing to the lack of a strong interaction between the support and ILs. Meanwhile, in the covalent bonding method, both the loading amount of ILs and their leaching are reduced. As a promising way to increase the loading of ILs on the support and at the same time reduce their leaching, polymeric or poly(ionic liquids) (PILs) have been recently introduced in which IL units are repeated as the monomer in a polymeric backbone.⁸ Polymerization of ILs means that in addition to the properties of ILs, polymeric properties such as high mechanical stability, permanent and strong polyelectrolytes, wide glass transition temperature (T_g), and solubility in polar and nonpolar solvents are also added to the composition.⁹ Recently, many reports have been directed towards the preparation of catalysts based on PILs because of their interesting combined features.^{10,11} For example, in a report by Zhao *et al.*, they prepared an easily recoverable PIL catalyst by sol-gel and ATRP polymerization methods for dye degradation.¹²

Recently, the design of organic-inorganic PIL composites with a network structure has become a new approach in this field to expand the benefits of the prepared compounds. In these nano-architectures, ILs are placed as organic interfacing materials between inorganic nanoparticles and they provide surface connections of nanoparticles to each other to form a network structure. These hybrid materials are called ionic network nanoparticles (INNs).¹³ In fact, INNs present a multi-dimensional form of ionic nanoparticles, which may have the potential of presenting many combined and interesting properties such as high ionic density and a flexible backbone. More importantly, these engineered nano-structures provide the possibility of protecting the nanoparticles from aggregation and stabilizing the ILs against leaching simultaneously. These exciting features, which are not commonly found in their non-network counterparts or in simple surface-modified materials with ILs, enable a wide range of applications across various scientific disciplines, including electronics, magnetism, and photonics.¹⁴ For the first time, Neouze *et al.* elegantly prepared INNs employing silica nanoparticles as seeds and an imidazolium based-IL as an ionic linker by two different methods.¹⁵ Afterwards, different nanoparticles such as TiO_2 and ZrO_2 were employed as supports in the production of the same INNs by the same research group.¹⁶

Recently, the use of magnetic nanoparticles (MNPs) has been expanded in a broad range of areas due to their remarkable properties such as convenient synthesis from inexpensive precursors, non-toxicity and good dispersibility.¹⁷ They have also attracted special attention in the field of catalysis for providing an easily recoverable catalytic system using only an external magnet.^{18,19} Although there are many reports on the functionalization of MNPs with ILs,²⁰⁻²² the application of MNPs to provide an INN structure has only been introduced

recently.²³ We have recently developed, for the first time, the design of a novel magnetic ionic network nanoparticle (MINN) structure comprising ultrasmall iron oxide nanoparticles as seeds and an imidazolium-based IL as an interfacing organic linker as an efficient support material with high ionic density to immobilize active Pd species.²⁴ While our previous MINN system successfully stabilized palladium nanoparticles and demonstrated high efficiency in the Suzuki reaction, attributed to its relatively high ionic density and flexibility, we hypothesize that additional enhancements in the hydrophobic-hydrophilic balance and stability, alongside an increase in ionic density, may be essential for achieving optimal performance in acidic environments to facilitate acid-catalyzed reactions. To do this, herein, we developed the synthesis of a new task-specific IL that incorporates three imidazolium moieties per MNP unit. This IL is designed to immobilize on the support through three distinct covalent connections, thereby facilitating the formation of a highly stable network structure at the molecular level. Therefore, the synthesized IL was covalently anchored to the surface of silica-coated iron oxide MNPs *via* a mercaptopropyl linker, utilizing a polymerization method to establish a novel hyper-branched and covalently bonded MINN structure. We hypothesize that the newly developed MINN system may exhibit enhanced chemical stability in harsh acidic environments, thereby advancing our previously outlined objectives and positioning it as a promising candidate for application as a support material in acid-catalyzed reactions. In order to test our hypothesis, we conducted a case study examining the performance of the synthesized MINN in immobilizing acidic species (HSO_4^-). In addition, we explored the application of the resulting material as a recoverable catalyst for the esterification of alcohols.

The direct esterification of alcohols with carboxylic acids represents a significant reaction in both academic and industrial settings, especially due to its recent applications in the synthesis of biofuels, pharmaceutical intermediates, fine chemicals, and polymer precursors.²⁵⁻³⁰ Traditionally, this reaction proceeds with homogeneous acid catalysts, which present considerable limitations, such as corrosiveness, environmental hazards associated with the disposal of acidic waste, and challenges related to the separation and recovery of the catalyst. To address these issues, supported acid catalysts, particularly those utilizing nanostructured materials, have emerged as effective and reusable alternatives. These catalysts encompass acidic ionic liquids immobilized on nanoscale supports, porous materials (*e.g.*, MCM-41, SBA-15, and metal-organic frameworks (MOFs)) that are functionalized with sulfonic groups, heteropolyacids supported on metal oxides or polymers, and polymer-supported Brønsted acids.³¹⁻³⁵ The main features of solid acid catalysts rely on their high surface area, improved accessibility of acidic sites, potential for recyclability, and adjustable acidity. These characteristics collectively contribute to the enhanced reaction rates and yields of products under milder and more environmentally sustainable conditions. Additionally, their heterogeneous nature allows for easy separation and reuse, aligning well with the principles of

sustainable catalysis. Meanwhile, the nanoscale architecture of these materials also promotes efficient mass transport and improved substrate–catalyst interactions. Nonetheless, equilibrium constraints in direct esterification reactions remain a significant challenge. Most supported acid catalysts developed thus far lack suitable surface functionalities that can effectively remove the water by-product, thereby limiting reaction yields or deactivating the catalytic acidic sites. In this context, we hope that the acid-functionalized MINN material developed in this study offers a promising solution. We predict that by combining highly accessible and active acidic sites within a uniformly distributed network, a strongly ionic nano-heterostructure, and surface hydrophobicity, this material creates a well-organized nanoscale and water-tolerant catalytic system to improve the overall reaction efficiency during the esterification of alcohols.

Experimental

Materials and instruments

All chemicals including sodium dodecylbenzenesulfonate (SDBS), $\text{FeCl}_2 \cdot 4\text{H}_2\text{O}$, $\text{Fe}(\text{NO}_3)_3 \cdot 9\text{H}_2\text{O}$, hydrazine 34%, tetraethyl orthosilicate (TEOS), (3-mercaptopropyl)trimethoxysilane, 1-vinylimidazole, 1,3,5-tris(bromomethyl)benzene, and azobisisobutyronitrile (AIBN) and also solvents were purchased from Merck, Sigma-Aldrich and Across Company. Philips CM-200 and Titan Krios TEMs were utilized for studying the structure of the synthesized material. TGA was performed from room temperature to 800 °C under a nitrogen or oxygen flow using a NETZSCH STA 409 PC/PG instrument. Nitrogen sorption analysis was obtained using a BELSORP-BELMAX instrument, Japan. FTIR spectra were recorded using a Bruker Vector 22 FTIR spectrometer. The magnetic properties were recorded using a homemade VSM (Meghnatis Daghigh Kavir Company, Iran) at room temperature from $-10\,000$ to $+10\,000$ Oe. Gas chromatography analyses were performed with a Varian CP-3800 system using a flame ionization detector (FID). ^1H -NMR and ^{13}C -NMR spectra were recorded using DMX-250 and DMX-400 MHz Bruker Avance spectrometers.

Synthesis of core–shell MNPs

Core–shell $\text{Fe}_3\text{O}_4@/\text{SiO}_2$ MNPs were synthesized *via* the microemulsion method in reverse water-in-oil micelles of SDBS as a surfactant.³⁶ In this method, first, SDBS (5 mmol, 1.75 g) was dissolved in xylene (15 ml) and sonicated for 30 min. An aqueous solution of iron salts containing $\text{FeCl}_2 \cdot 4\text{H}_2\text{O}$ (0.75 mmol) and $\text{Fe}(\text{NO}_3)_3 \cdot 9\text{H}_2\text{O}$ (1.5 mmol) in deionized water (0.75 ml) was prepared. The prepared aqueous solution was added to the oil solution under vigorous stirring. The microemulsion was stirred for 12 hours at room temperature. In the next step, the microemulsion temperature was slowly raised to 90 °C for an hour and placed under reflux and argon gas. When the temperature stabilized at 90 °C, aqueous hydrazine solution (1 ml, 34 wt%) was injected dropwise into the reaction mixture to form a black precipitate of Fe_3O_4 . After 3 hours of

vigorous stirring under the flow of argon gas, the mixture was cooled down to 40 °C in an hour. To form a silicate shell around the magnetic core of Fe_3O_4 , TEOS (9 mmol, 2 ml) was added dropwise to the mixture and stirred at 40 °C for 15 hours under the flow of argon gas. At the end, the prepared MNPs were collected using a magnet and washed with deionized water and ethanol until the surfactant was completely removed. The material was dried at 80 °C in an oven and finally a reddish-brown powder was obtained (Fig. S1†).

Immobilization of (3-mercaptopropyl)trimethoxysilane on the MNPs

An aqueous solution containing (3-mercaptopropyl)trimethoxysilane (1.68 mmol, 0.33 g), ethanol (14 ml) and deionized water (14 ml) was added to a 50 ml flask containing 0.4 g of MNPs and sonicated for 30 min. The reaction was completed by stirring under refluxing conditions at 80 °C under an argon atmosphere for 24 hours. The supported MNPs were collected using an external magnet and thoroughly washed using ethanol and deionized water several times. $\text{Fe}_3\text{O}_4@/\text{SiO}_2\text{-SH}$ was finally dried at 80 °C in an oven overnight (Fig. S2†).

Synthesis of 1,3,5-tris(vinyl imidazole methyl)benzene bromide

To prepare the 1,3,5-tris(vinyl imidazole methyl)benzene bromide IL, 1-vinylimidazole (15 mmol) was first added to a 100 mL flask under an argon atmosphere. Then, dry toluene (30 mL) was added to the flask, followed by the addition of 1,3,5-tris(bromomethyl)benzene to the reaction mixture. The temperature was then raised to 100 °C, and the solution was stirred under reflux for 24 hours. After cooling, the reaction mixture was first washed with ethyl acetate (2×50 mL), followed by washing with diethyl ether (2×50 mL). Finally, the prepared IL was placed in an oven at 70 °C to dry (Fig. S3†). White powder, ^1H NMR (400 MHz, DMSO) $\delta_{\text{H}} = 9.90$ (s, 1H), 8.33 (s, 1H), 8.07 (s, 1H), 7.72 (s, 1H), 7.41 (dd, 1H), 6.06 (d, 1H), 5.56 (s, 2H), 5.46 (dd, 1H), 2.52 (s, 2H); ^{13}C NMR (101 MHz, DMSO) $\delta_{\text{C}} = 136.21, 129.85, 129.33, 123.90, 119.88, 109.44, 52.07, 40.00$.

Immobilization of the IL on $\text{Fe}_3\text{O}_4@/\text{SiO}_2\text{-SH}$

$\text{Fe}_3\text{O}_4@/\text{SiO}_2\text{-SH}$ (0.3 g), the prepared IL (0.18 mmol, 0.113 g) and dry ethanol (20 ml) were added to a 50 ml flask. The reaction mixture was sonicated for 30 min. In the next step, AIBN (0.18 mmol, 30 mg) was added to the flask under argon gas. The temperature was then raised and the solution was stirred under reflux and an argon atmosphere for 24 hours. A magnet was used to separate the prepared material. The material was thoroughly washed using ethanol and dichloromethane. $\text{Fe}_3\text{O}_4@/\text{SiO}_2\text{-S-xIm}^+\text{Br}^-$ was finally dried at 70 °C in an oven (Fig. S4†).

Preparation of $\text{Fe}_3\text{O}_4@/\text{SiO}_2\text{-S-xIm}^+\text{HSO}_4^-$

The final catalyst was prepared by a simple method using an ion exchange protocol. First, a saturated aqueous solution of potassium hydrogen sulfate was prepared. In the next step,

$\text{Fe}_3\text{O}_4@\text{SiO}_2\text{-S-xIm}^+\text{Br}^-$ (200 mg) and the prepared saturated solution of KHSO_4 (5.2 ml) were added to a 10 ml flask and sonicated for 30 min. To exchange the bromide anion with the hydrogen sulfate anion, the obtained mixture was stirred at room temperature for 24 hours. Finally, $\text{Fe}_3\text{O}_4@\text{SiO}_2\text{-S-xIm}^+\text{HSO}_4^-$ was separated using an external magnet and washed using deionized water several times and dried at 80 °C in an oven (Fig. S5†).

Determination of hydrogen sulfate anion loading

The back titration method was used to determine the amount of acid loading. In this way, $\text{Fe}_3\text{O}_4@\text{SiO}_2\text{-S-xIm}^+\text{HSO}_4^-$ (100 mg) and a saturated solution of NaCl (20 ml) were added to a 50 ml flask and stirred for 6 hours. After this, the catalyst was separated using a magnet, and the remaining solution was subjected to titration. The remaining solution was transferred to a flat-bottom flask and a drop of phenolphthalein indicator was added to it. Then some amount of 0.01 M standard NaOH solution was added to the mixture until its color turned purple and titrated with 0.01 M standard HCl solution. The endpoint of the titration is when the purple color changes to colorless. The obtained values were placed in the following formula:

$$\{(M_{\text{NaOH}} \times V_{\text{NaOH}}) - (M_{\text{HCl}} \times V_{\text{HCl}})\} \times 1000.$$

General procedure for the solvent-free esterification reaction of primary and secondary alcohols with acetic acid

A 5 ml round-bottom flask was charged with alcohol (1 mmol), acetic acid (5–7 mmol) and $\text{Fe}_3\text{O}_4@\text{SiO}_2\text{-S-xIm}^+\text{HSO}_4^-$ (0.1 mol%), and then stirred at 85 °C for 15–40 hours. After the completion of the reaction, the mixture was cooled down to room temperature and the catalyst was separated using an external magnet. The product was diluted with ethyl acetate, dried with sodium sulfate and analyzed using GC (gas chromatography).

Catalyst recovery in the solvent-free esterification reaction of 1-octanol and acetic acid

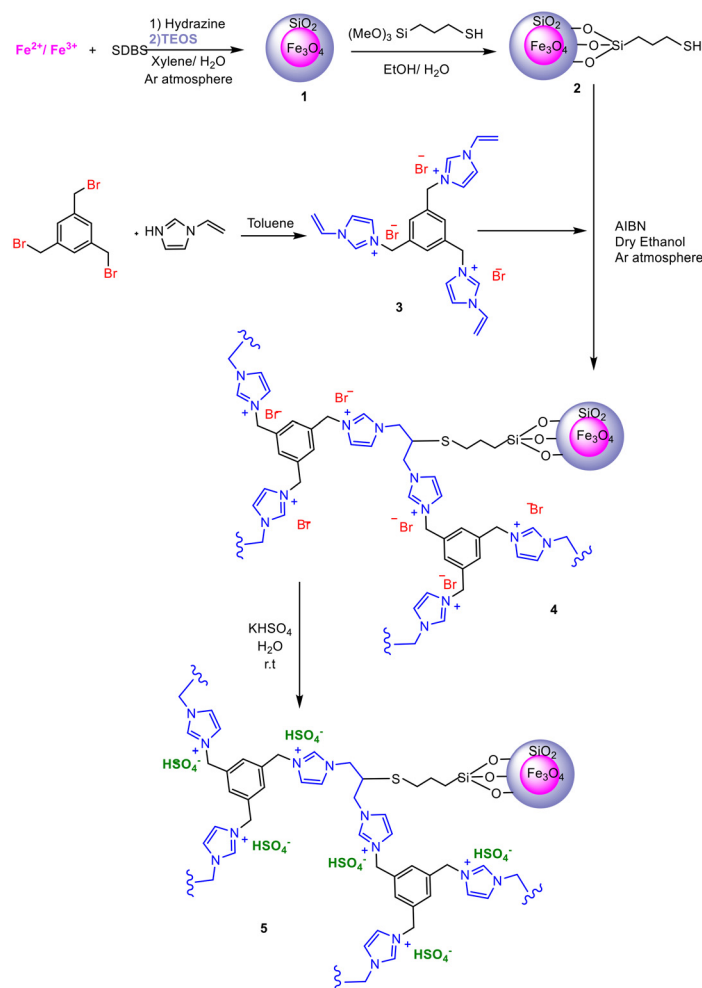
A mixture of 1-octanol (1 mmol), acetic acid (5 mmol) and $\text{Fe}_3\text{O}_4@\text{SiO}_2\text{-S-xIm}^+\text{HSO}_4^-$ (0.1 mol%) was prepared in a 5 ml flask. The resulting mixture was stirred at 85 °C for 15 hours. After the completion of the reaction, the mixture cooled to room temperature, and the catalyst was separated using an external magnet and washed 5 times with ethyl acetate. In the next cycle, the reactants were added to the flask, and the reaction was repeated under the same conditions. The progress of the reaction in each cycle was monitored by GC.

Results and discussion

The catalyst was prepared *via* the procedure presented in Scheme 1 in a few steps: initially, Fe_3O_4 nanoparticles were prepared by a known water-in-oil microemulsion method in the presence of SDBS as a surfactant followed by the addition of TEOS to create a silica shell.³⁶ The microemulsion method

was employed because it provides appropriate control over the shape, size, morphology and silica thickness of nanoparticles.³⁷ The narrow and uniform size distribution of $\text{Fe}_3\text{O}_4@\text{SiO}_2$ core-shell nanoparticles **1**, utilized as inorganic seeds, will facilitate the appropriate three-dimensional homogeneity in the hybrid organic-inorganic ionic network that we have developed.

Next, (3-mercaptopropyl)trimethoxysilane was utilized as a linker and grafted onto **1** to give $\text{Fe}_3\text{O}_4@\text{SiO}_2\text{-SH}$ **2**, soon after facilitating the connection of the IL to the surface in the subsequent stages. In the following step, 1,3,5-tris(vinyl imidazole methyl)benzene bromide **3**, which possesses triple binding capability, was synthesized through a simple nucleophilic substitution. This was followed by a reaction with **3** *via* a radical polymerization method, employing AIBN as an initiator in dry ethanol under an argon atmosphere to produce $\text{Fe}_3\text{O}_4@\text{SiO}_2\text{-S-xIm}^+\text{Br}^-$ **4**. Subsequently, to synthesize the final catalyst $\text{Fe}_3\text{O}_4@\text{SiO}_2\text{-S-xIm}^+\text{HSO}_4^-$ **5**, the bromide anion was substituted with the hydrogen sulfate anion through an ion exchange process conducted in water at ambient temperature (Scheme 1). The materials prepared in each step were characterized using a variety of techniques, including TGA, FTIR, N_2 adsorption-desorption, CHNS elemental analysis, TEM, and VSM. TGA conducted over a range of 25–800 °C was used to estimate the organic content and the thermal stability of the immobilized organic groups in the prepared materials (Fig. 1 and S6–S8†). The TG diagram of **2** shows thermal stability up to about 250 °C. The weight loss observed at around 300 °C is related to the thermal degradation of the mercaptopropyl group (Fig. 1a). As observed in the TG diagram of **4** and **5** (Fig. 1b and c), the thermal stability of the materials is still in the range of 250–300 °C, indicating the high thermal stability of the immobilized polymer network on the support. This high thermal stability, to a great extent, could be attributed to the formation of a 3D network structure in the materials and originates from the strong covalent bonding of imidazolium moieties *via* multiple sites to the support. Based on the DTG diagram (Fig. S7†), the main weight loss of **4** is centered at a temperature of about 330 °C. Catalyst **5** showed a comparable high thermal stability, exceeding 300 °C. This observation indicates that the treatment of the support with an acidic medium did not alter its structural integrity or chemical stability (Fig. 1c and S8†). The TG weight loss of $\text{Fe}_3\text{O}_4@\text{SiO}_2\text{-SH}$, $\text{Fe}_3\text{O}_4@\text{SiO}_2\text{-S-xIm}^+\text{Br}^-$, and $\text{Fe}_3\text{O}_4@\text{SiO}_2\text{-S-xIm}^+\text{HSO}_4^-$ was measured at 6.8%, 18.2%, and 19.6%, respectively. These findings are consistent with the increasing proportion of the organic component in the synthesized composite. The loading amounts of the mercaptopropyl group and ionic liquid (IL) were determined to be 0.9 mmol g^{−1} and 0.53 mmol g^{−1}, respectively, based on the weight loss of each component. However, the inability to distinguish between the weight losses of different functionalities in the thermogravimetric (TG) diagrams introduces a significant degree of uncertainty in the calculated loadings derived from this method. Therefore, to obtain more accurate information regarding the elemental composition and the loading of functional groups in the syn-



Scheme 1 General procedure for the synthesis of (1) $\text{Fe}_3\text{O}_4@\text{SiO}_2$ MNPs, (2) $\text{Fe}_3\text{O}_4@\text{SiO}_2\text{-SH}$, (3) 1,3,5-tris(vinyl imidazole methyl)benzene bromide (IL), (4) $\text{Fe}_3\text{O}_4@\text{SiO}_2\text{-S-xIm}^+\text{Br}^-$ and (5) $\text{Fe}_3\text{O}_4@\text{SiO}_2\text{-S-xIm}^+\text{HSO}_4^-$.

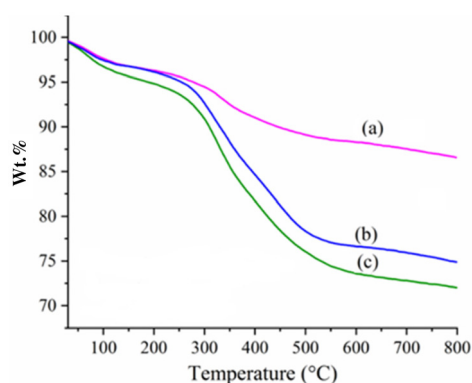


Fig. 1 TG analysis of $\text{Fe}_3\text{O}_4@\text{SiO}_2\text{-SH}$, **2** (a); $\text{Fe}_3\text{O}_4@\text{SiO}_2\text{-S-xIm}^+\text{Br}^-$, **4** (b); and $\text{Fe}_3\text{O}_4@\text{SiO}_2\text{-S-xIm}^+\text{HSO}_4^-$, **5** (c).

thesized materials, a stepwise CHNS elemental analysis was conducted. The results are summarized in Table S1.†

Based on the sulfur content (2.06%) determined through elemental analysis, the loading of the mercaptopropyl group

was calculated to be 0.64 mmol g^{-1} in sample **2**. In the case of the CHNS analysis of sample **4**, the significant increases in the percentages of carbon (9.63%) and nitrogen (2.10%) compared to the values observed in sample **2** provide compelling evidence for the successful incorporation of the polymeric ionic liquid (PIL) onto the surface of sample **4**. In this way, the loading of IL was calculated to be 0.75 mmol g^{-1} based on the N% in **4**. Finally, elemental analysis of **5** demonstrated a remarkable increase in sulfur content compared to that of **4** (from 2.12 to 3.76%), confirming the successful ion-exchange of Br^- with HSO_4^- . Based on the increase in sulfur content, the loading of HSO_4^- was estimated to be 0.51 mmol g^{-1} in the final catalyst **5**. Furthermore, the loading amount of the hydrogen sulfate anion in the final catalyst was found to be 0.47 mmol g^{-1} , using the back titration method, which is consistent with the value obtained from the elemental analysis.

N_2 adsorption-desorption analysis was also used to get information about the structure and surface area of the synthesized material. According to the IUPAC classification, all compounds demonstrated a type IV absorption-desorption iso-

therm with an H1 hysteresis loop at high relative pressures (above 0.8), which indicates the absorption of nitrogen gas in the space of macropores or inter-particle spaces (Fig. S9–S12†). The surface area of materials 1, 2, 4, and 5, calculated using the BET method, was found to be 255, 87, 74 and 52 m² g^{−1}, respectively (Fig. S9–S12†). The stepwise decrease in the surface area indicates the successful immobilization of functional groups in each step. However, the total structure of the isotherm was not manipulated upon treatment of the support with an acidic medium, confirming the high stability of the 3D network.

The FT-IR spectra (Fig. 2) of all compounds have shown peaks related to stretching vibrations of the Fe–O bond (500 cm^{−1}), symmetric and asymmetric stretching of the Si–O–Si bond and the stretching vibration of Si–OH (800 and 1300 cm^{−1}, respectively), which indicate the presence of Fe₃O₄ and SiO₂ phases in all materials (for more details, please see Fig. S13–S16†).²¹ In the FT-IR spectra of 2 (Fig. S14†), the peak observed at around 600 cm^{−1} is related to the C–S stretching vibration, which presents the successful immobilization of the (3-mercaptopropyl)trimethoxysilane group. In addition to the peaks mentioned above, the stretching vibration of C=C (1570 cm^{−1}) and the stretching vibration of C=N (1625 cm^{−1}) as well as the stretching vibration of aliphatic and aromatic C–H bonds can be seen in the FT-IR spectrum of Fe₃O₄@SiO₂-S-xIm⁺Br[−] (Fig. S15†), which confirms the successful covalent anchoring of the aromatic polymeric backbone consisting of the imidazolium IL on the MNPs. Furthermore, the presence of the symmetric and asymmetric O=S=O stretching vibration peaks (1030–1168 cm^{−1}) and the stretching vibration peaks (3300–3400 cm^{−1}) of the hydroxyl group in the FTIR spectrum of the Fe₃O₄@SiO₂-S-xIm⁺HSO₄[−] specify the successful implementation of the ion exchange process (Fig. S16†).

The high-resolution TEM (HRTEM) technique was employed to gain insight into the shape and morphology of

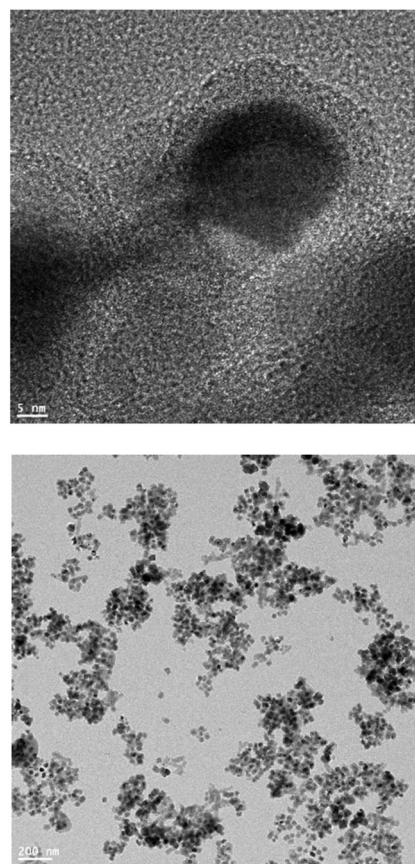


Fig. 3 HRTEM (up) and TEM (down) images of the Fe₃O₄@SiO₂-S-xIm⁺HSO₄[−] catalyst.

the prepared catalyst (Fig. 3). The HRTEM image of the catalyst displayed the spherical shape and core-shell structure of the Fe₃O₄@SiO₂ support (Fig. 3, top). The darker area is the Fe₃O₄ nanoparticles as the core, which is coated with uniform bright silica and an organic layer as the shell. The approximate diameter of the Fe₃O₄ core is 20 nm and the thickness of the coating materials is in the range of 5–7 nm. The long-view TEM image of the prepared catalyst (Fig. 3, bottom) showed that after the stepwise immobilization of mercaptopropyl and IL units followed by ion exchange in an acidic medium, the uniformly distributed core-shell structure is preserved and no appreciable agglomeration of nanoparticles is observed. Also, the image of the catalyst displays that the nanoparticles are placed close to each other in a regular pattern and a chain-like arrangement. This observation could be considered as evidence for forming the network structure in the prepared material.²⁴

To study the magnetic behavior of the synthesized materials, VSM analysis was conducted at room temperature (Fig. 4 and Fig. S17–S20†). The results indicate that all materials displayed no hysteresis loop, thereby confirming their superparamagnetic behavior.²¹ The saturation magnetization values of 1, 2, 4, and 5 were found to be 24.5, 21, 20 and 15 emu g^{−1}, respectively. The gradual reduction in the mag-

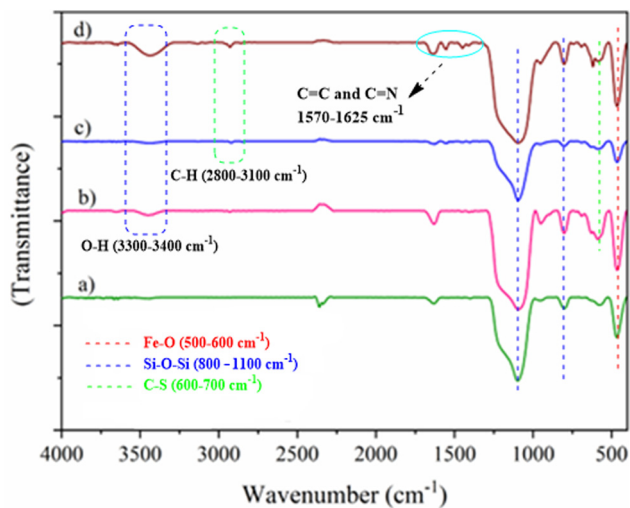


Fig. 2 FT-IR spectra of Fe₃O₄@SiO₂ (a), Fe₃O₄@SiO₂-SH (b), Fe₃O₄@SiO₂-S-xIm⁺Br[−] (c) and Fe₃O₄@SiO₂-S-xIm⁺HSO₄[−] (d).

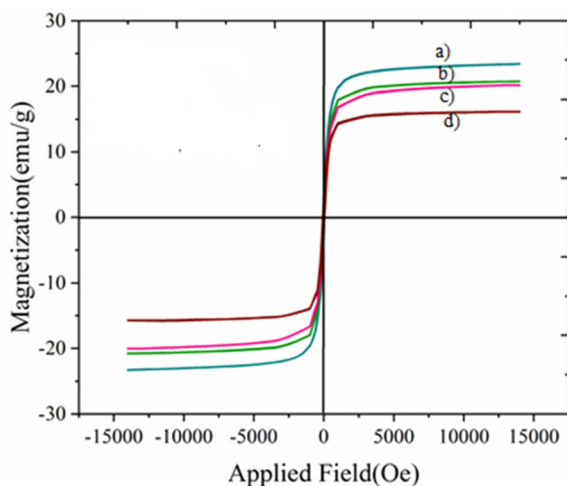


Fig. 4 VSM curves of $\text{Fe}_3\text{O}_4@\text{SiO}_2$ (a), $\text{Fe}_3\text{O}_4@\text{SiO}_2\text{-SH}$ (b), $\text{Fe}_3\text{O}_4@\text{SiO}_2\text{-S-xlm}^+\text{Br}^-$ (c) and $\text{Fe}_3\text{O}_4@\text{SiO}_2\text{-S-xlm}^+\text{HSO}_4^-$ (d).

netic saturation value in a stepwise manner signifies the successful functionalization of magnetic support in each stage, which is consistent with the diminishing proportion of the magnetic core within the composite. In the final step, when the anion of the ionic liquid (IL) is substituted with the hydrogen sulfate anion (Fig. S20[†]), a notable decrease in the degree of magnetic saturation is observed compared to the preceding steps. This reduction may be partially attributed to the minor degradation and/or dissolution of the magnetic core in the aqueous acidic solution. Nevertheless, the magnetic saturation value of the final catalyst remains significantly high at 15 emu g^{-1} , facilitating its complete and rapid separation from the reaction environment through the application of an external magnet.

After a comprehensive characterization of the catalyst, its catalytic activity was explored in the esterification of alcohols under solvent-free conditions. First, the catalytic performance of catalyst 5 was examined in the esterification reaction involving 3-phenyl-1-propanol and acetic acid to find the optimum reaction conditions. To do this, the impacts of various parameters, including the reaction temperature and time, the ratio of acetic acid to alcohol, and the quantities of the catalyst, were precisely assessed (Table S2[†]). Initially, the reaction was conducted in the presence of 5 mol% of the catalyst at a temperature of 45°C , using 2.5 equivalents of acetic acid. The results showed that the product yield progressively increased by extending the reaction time and reached the maximum yield of 76% after 40 hours (Table S2, [†] entries 1–3). In light of these results, we decided to check the reaction at higher temperatures while utilizing lower amounts of the catalyst in an effort to obtain higher yields (Table S2, [†] entries 4–8). After conducting several analyses, we observed that the reaction achieved a yield of 98% at a temperature of 75°C with the use of 1 mol% of the catalyst. Furthermore, a quantitative yield of the product (100%) was obtained at 85°C with as low as 0.5 mol% of catalyst 5 after 40 hours (Table S2, [†] entries 6 and

8). It seems that the removal of the water by-product from the vicinity of catalytic sites may contribute to an enhancement in yield at elevated temperatures. Following the observation of favorable results with reduced catalyst quantities at 85°C , we performed a series of kinetic experiments to monitor the reaction progress at various time intervals, using low catalyst loadings of 0.5 and 0.2 mol% under the same reaction conditions (Table S2, [†] entries 9–29). Based on this survey, complete reaction conversion was achieved after 30 h and 40 h when utilizing 0.5 and 0.2 mol% of catalyst 5, respectively (Table S2, [†] entries 14 and 29). In the next stage, we noted that reducing the quantity of acetic acid from 2.5 to 1.5 equivalents led to a decrease in the reaction yield (Table S2, [†] entries 30 and 31). Conversely, we observed that increasing the amount of acetic acid to 5 equivalents resulted in a significant enhancement in the reaction progress, which was completed within 15 hours, even with a minimal catalyst loading of 0.2 mol% at a temperature of 85°C (Table S2, [†] entries 32–39). Along with these remarkable results, we decided to further reduce the amount of the catalyst under the same reaction conditions (Table S2, [†] entries 40 and 41). Notably, we observed that by using as low as 0.1 mol% of the catalyst and 5 equivalents of acetic acid, the reaction proceeded with nearly quantitative yield after 15 h. It should be emphasized that achieving the quantitative yield using such a low catalyst quantity in the esterification of alcohols is a significant outcome that has previously been largely elusive. Consequently, the conditions established in entry 40 of Table S2[†] were chosen as the optimal conditions for the subsequent studies.

Having the optimal reaction conditions in hand, the activity of catalyst 5 was investigated in the esterification reaction of a series of primary aromatic and aliphatic alcohols with acetic acid to explore the substrate scope of the process. In general, it can be stated that alcohol acts as a nucleophile in the esterification reaction; thus, the weaker the alcohol nucleophile, the lower the efficiency of the reaction. Various factors, including the electronic properties and the steric hindrance of the alcohol, influence its nucleophilic characteristics and, consequently, diminish its reactivity in the esterification process. The catalyst was first employed in the reaction of long-chain aliphatic alcohols (Table 1). The results showed that the catalyst exhibited remarkable activity and efficiency in the esterification reactions of aliphatic alcohols with varying chain lengths, specifically from 1-heptanol to 1-dodecanol, yielding quantitative yields of the corresponding acetate ester for all substrates under optimized reaction conditions (Table 1, entries 1–5). In addition, the catalyst showed high efficiency (>99% yield) in the esterification of cinnamyl alcohol as an allylic alcohol under optimal conditions (Table 1, entry 7).

Remarkably, a wide variety of primary benzylic alcohols bearing either electron-donating or electron-withdrawing groups at the *para* and/or *ortho* position gave good to excellent yields under the optimized reaction conditions (Table 1, entries 8–16). Alcohols possessing an electron-donating group at the *para* position gave quantitative yields under optimal conditions (see Table 1, entries 9 and 10). In contrast, the

Table 1 Direct esterification of primary alcohols with acetic acid using the $\text{Fe}_3\text{O}_4@\text{SiO}_2\text{-S-xIm}^+\text{HSO}_4^-$ catalyst

$\text{R-OH} + \text{HO-C(=O)-CH}_3 \xrightarrow[85^\circ\text{C, 15 h}]{\text{5 (0.1 mol\%)}} \text{RO-C(=O)-CH}_3$			
Entry	Alcohol	Yield (%)	TON
1	1-Heptanol	>99	990
2	1-Octanol	>99	990
3	1-Nonanol	>99	990
4	1-Decanol	>99	990
5	1-Dodecanol	>99	990
6	3-Phenyl-1-propanol	>99	990
7	Cinnamyl alcohol	>99	990
8	Benzyl alcohol	95	950
9	4-Methylbenzyl alcohol	97	970
10	4-Methoxybenzyl alcohol	>99	990
11	4-Chlorobenzyl alcohol	95	950
12	2,4-Dichlorobenzyl alcohol	94	940
13	4-Nitrobenzyl alcohol	86	860
14	2-Nitrobenzyl alcohol	80	880
15	3-Pyridinyl methanol	95	950
16	1-Naphthyl methanol	>99	990

Reaction conditions: alcohol: 1 mmol; acetic acid: 5 mmol; solvent-free; yields are based on GC.

efficiency of benzylic alcohols containing electron-withdrawing groups at either the *ortho* or *para* positions was marginally lower than that of alcohols with electron-donating groups. Nevertheless, the catalyst exhibited remarkable activity in facilitating the production of the corresponding esters with high yields (Table 1, entries 11–14). This observation could be attributed to the lower nucleophilicity of alcohols having electron-withdrawing groups. In particular, in the case of alcohols bearing the electron-withdrawing group in the *ortho* position, which is hindered both sterically and electronically, did not significantly diminish the reaction efficiency (Table 1, entries 12 and 14). In addition, both heteroatom-containing alcohols and bulky 1-naphthyl methanol, which exhibit reduced nucleophilic properties, afforded the corresponding esters in excellent yields (Table 1, entries 15 and 16). A notable advantage of the current catalytic system is its effective response to a diverse array of primary alcohols, coupled with a significantly lower catalyst consumption compared to other systems. This efficiency has resulted in high turnover numbers (TONs) in the present investigation (Table 1).

After successful application of the prepared $\text{Fe}_3\text{O}_4@\text{SiO}_2\text{-S-xIm}^+\text{HSO}_4^-$ catalyst for the esterification of primary alcohols, we turned our attention towards the transformation of more challenging secondary alcohols to the corresponding esters. Secondary alcohols are even weaker nucleophiles compared to primary alcohols, primarily due to their increased steric hindrance. As a consequence, they exhibit reduced reactivity in esterification reactions. Therefore, more rigorous conditions are often required to achieve a high yield of the desired product. In addition, in certain cases involving secondary alcohols, the etherification reaction may occur as an unintended side reaction. Consequently, it is generally essential to re-opti-

mize the reaction conditions to ensure both high yield and selectivity of the process. Thus, prior to investigating the various secondary alcohols as substrates, we re-checked the influence of reaction parameters, including the quantity of the catalyst, the reaction time, and the amount of acetic acid, on the reaction yield (Table S3†). In this way, the esterification reaction of cyclohexanol with acetic acid was examined as a model reaction under previously optimal conditions for primary alcohols. The results showed a moderate yield of 55% (Table S3,† entry 1). Subsequent experiments revealed that increasing the quantity of catalyst 5, as well as extending the reaction time, did not result in any noticeable improvement in the reaction efficiency (Table S3,† entries 2–6). Subsequently, for further investigation, the effect of 7 and 10 equivalents of acetic acid was examined, and the reaction was monitored at various time intervals (Table S3,† entries 7–14). The results showed that the use of 7 equivalents of acetic acid is sufficient to give a satisfactory yield of the product while utilizing only 0.1 mol% of catalyst 5. Ultimately, the optimal reaction conditions were determined to be 0.1 mol% of the catalyst, a temperature of 85 °C, a reaction time of 24 hours, and a molar ratio of 1 : 7 for alcohol to acetic acid (Table S3,† entry 11).

Under the optimal conditions, esterification reactions of various aliphatic and aromatic secondary alcohols with acetic acid were explored (Table 2). In the case of cyclic aliphatic alcohols, it was noted that as the number of carbons increases, the yield of the reaction exhibits a moderate decrease; however, the yield of all related products still remains excellent (Table 2, entries 1–3). Additionally, good yields were also obtained when using long-chain aliphatic secondary alcohols as substrates under the optimal reaction conditions (Table 2, entries 4 and 5). In contrast, secondary benzylic alcohols exhibit somewhat lower efficiency due to their reduced nucleophilicity and increased steric hindrance, necessitating extended reaction times to obtain satisfactory yields (Table 2, entries 6 and 7). Gratifyingly, catalyst 5 demonstrated remarkable efficiency, even when using highly hindered aliphatic alcohols, such as borneol, as a substrate, fur-

Table 2 Direct esterification reaction of secondary alcohols with acetic acid using the $\text{Fe}_3\text{O}_4@\text{SiO}_2\text{-S-xIm}^+\text{HSO}_4^-$ catalyst

$\text{R}^1\text{-CH(OH)-R}^2 + \text{HO-C(=O)-CH}_3 \xrightarrow[85^\circ\text{C}]{\text{5 (0.1 mol\%)}} \text{R}^1\text{-CH(O-C(=O)-CH}_3\text{)-R}^2$			
Entry	Alcohol	Yield (%)	TON
1	Cyclohexanol	90	900
2	Cycloheptanol	88	880
3	Cyclooctanol	85	850
4	2-Heptanol	89	890
5	2-Octanol	91	910
6 ^a	1-Phenylethanol	86	860
7 ^a	1-Phenyl-1-propanol	78	780
8	Borneol	95	950

Reaction conditions: alcohol: 1 mmol; acetic acid: 7 mmol; solvent-free, 24 h; yields are based on GC. ^a Reaction time: 40 h.

nishing an impressive yield of 95% (Table 2, entry 8). It should be again highlighted that the above-mentioned promising results could be obtained using only 0.1 mol% of **5**. It is noteworthy that the selectivity of the ester products in all cases was 100%, indicating the absence of any side reactions, such as etherification and/or elimination, in the process using the present catalyst. We speculate that the remarkable reactivity and selectivity of the developed catalyst can be attributed to the optimal distribution of highly active acidic sites across the meticulously designed three-dimensional PIL support. This configuration not only facilitates a nano-ionic-acidic reactor with accessible and highly active sites for the alcohols but also enhances the hydrophobic nature, which in turn accelerates the expelling of the water by-product from the vicinity of the reactive sites, thereby improving the overall reaction yield and the catalyst performance.

In the next part, we conducted a series of control experiments to evaluate both the actual active site and true efficacy of our developed catalyst system. To do this, we performed the esterification reaction of benzyl alcohol with acetic acid under the optimal conditions, utilizing the materials synthesized at each step of the catalyst production process, in addition to H_2SO_4 and KHSO_4 (Table 3). As shown in Table 3, the blank reaction proceeded smoothly and yielded only 43% of benzyl acetate after 15 hours (Table 3, entry 1). In the presence of **1** and **4**, the yield of the reaction did not exhibit a significant change compared to the blank reaction (Table 3, entries 4 and 5). Meanwhile, catalyst **5** gave an excellent yield of 95% of the ester adduct under the same reaction conditions (Table 3, entry 6). These findings suggest two important points: first, the HSO_4^- counter ion serves as the actual active site in this catalyst system and is primarily responsible for the high yield of the ester; second, leaching of iron species present in the core of the support into the solution is negligible and therefore cannot function as a Lewis acid catalyst. Notably, the present recoverable catalyst **5** demonstrated superior activity compared to sulfuric acid, which is a strong, corrosive, and non-recoverable acid that acts as a homogeneous catalyst (Table 3, entry 2 vs. 6). To check the actual role of the developed matrix in enhancing catalyst efficacy, we compared the reaction outcomes using either catalyst **5** or KHSO_4 , which

serves as a homogeneous counterpart of our synthesized catalyst (Table 3, entry 3 vs. 6). The results indicated that catalyst **5** exhibited significantly higher activity, despite having a comparable HSO_4^- content. This observation underscores the notion that while the support does not exert a direct chemical influence on the acid-catalyzed reaction, it may play a crucial role in establishing a suitable hydrophobic-hydrophilic micro-environment in close proximity to the active sites. As previously hypothesized, one proposal suggests that this configuration and matrix composition may facilitate the efficient diffusion of starting materials into the nanoscale spaces of the catalyst network, where the active sites are situated. Additionally, this arrangement may enable the rapid expulsion of water from the vicinity of the active sites, thereby contributing to a high-performance and durable catalyst system in the esterification reaction.

In the subsequent section of our study, we compared the solvent-free esterification reaction of benzyl alcohol with acetic acid utilizing catalyst **5** with previously reported heterogeneous acidic catalysts. As illustrated in Table 4, the present catalyst shows a high efficiency and is comparable with those of other catalysts. The main advantage of our catalyst system is its ability to perform the esterification reaction with very low catalyst loading, resulting in substantially higher TON and turnover frequency (TOF) values in comparison with other studies.

The ability of heterogeneous catalysts to be recycled and recovered through efficient and straightforward methods, along with their stability during successive reuse, are critical

Table 3 Control experiments to evaluate the actual role of catalyst components

Entry	Sample	Catalyst (mol%)	Yield (%)
1	Blank	—	43
2	H_2SO_4	0.1	90
3	KHSO_4	0.1	74
4 ^a	$\text{Fe}_3\text{O}_4@\text{SiO}_2$	—	44
5 ^a	$\text{Fe}_3\text{O}_4@\text{SiO}_2\text{-S-xIm}^+\text{Br}^-$	—	47
6 ^a	$\text{Fe}_3\text{O}_4@\text{SiO}_2\text{-S-xIm}^+\text{HSO}_4^-$	0.1	95

^a The same weight of each sample was employed as the catalyst.

Table 4 Comparing the catalytic activity of $\text{Fe}_3\text{O}_4@\text{SiO}_2\text{-S-xIm}^+\text{HSO}_4^-$ with other solid acid catalysts in the esterification reaction

Entry	Catalyst	Yield (%)	TON	TOF (h^{-1})	Ref.
1 ^a	$\text{IL}@\text{SBA-15-Pr-SO}_3\text{H}$	91	9.1	0.2	38
2 ^b	$\text{SO}_3\text{H}@\text{P-E15}$	97	194	12.1	39
3 ^c	$\text{Et-PMO-Me-PrSO}_3\text{H}$	99	99	4.1	40
4 ^d	$\text{PrSO}_3\text{H/SBA-15}$	99	247	49.4	41
5 ^e	$[\text{ChCl}][\text{CrCl}_3 \cdot 6\text{H}_2\text{O}]_2$	75	300	12.5	42
	DES				
6 ^f	SHBPAO	76	152	25.4	43
7 ^g	PAFR	96	137	11.4	44
8	$\text{Fe}_3\text{O}_4@\text{SiO}_2\text{-S-xIm}^+\text{HSO}_4^-$	95	950	63.3	This work

^a Reaction conditions: acetic acid (1.7 mmol), catalyst (10 mol%), 45 °C, 40 h, and 4 run recovery. ^b Reaction conditions: acetic acid (2 mmol), catalyst (0.5 mol%), 50 °C, 16 h, and 10 run recovery. ^c Reaction conditions: acetic acid (5 mmol), catalyst (1 mol%), 60 °C, 24 h, and 10 run recovery. ^d Reaction conditions: acetic acid (2 mmol), catalyst (0.4 mol%), 100 °C, 5 h, and 3 run recovery. ^e Reaction conditions: acetic acid (5 mmol), catalyst (0.25 mol%), r.t., 24 h, and 10 run recovery. ^f Reaction conditions: acetic acid (1 mmol), catalyst (0.5 mol%), 90 °C, 6 h, and 5 run recovery. ^g Reaction conditions: acetic acid (1.2 mmol), catalyst (0.7 mol%), 50 °C, and 12 h.

factors in the design and production of catalysts. Therefore, the next phase of this study is focused on evaluating the stability of the catalyst and its recovery during the reaction of 1-octanol and acetic acid under optimized reaction conditions. After each run, the catalyst was separated from the reaction vessel using a simple magnetic bar and subsequently washed with ethyl acetate to remove any products or residual reactants. The catalyst was then subjected to the next run without undergoing any additional washing or drying process. Observations indicated that the catalyst displayed excellent dispersibility in repeated reactions after separation from each run. Through this convenient and efficient recycling process, our catalyst was demonstrated to be recycled and reused in the esterification reaction for up to 10 runs without a significant decrease in the reaction yield.

To investigate the possible structural changes, the recovered catalyst after ten runs was analyzed with TGA, N_2 sorption analysis, FT-IR, CHNS, TEM and VSM. The TGA curve of the recycled catalyst after 10 cycles showed that it retains thermal stability up to 300 °C, with the weight loss observed being comparable to that of the fresh catalyst (Fig. S21 and S22†). This finding suggests that leaching of the IL species did not occur, even after ten cycles. These observations can be attributed to the tight binding of the IL species to the surface of the nanoparticles at multiple sites, which arises from the network structure. This strong interaction has resulted in excellent stability of the IL on the surface, which prevents leaching to a great extent even in a harsh acidic environment combined with elevated temperature (Fig. 5).

The observation of a type (IV) isotherm in the N_2 sorption analysis proves that the catalyst retained its overall structural integrity after the recycling procedure (Fig. S23†). The BET surface area of the recycled catalyst 5 was calculated to be 37 m² g⁻¹, which is slightly lower than that of the fresh catalyst. This decrease in the surface area may be attributed to the potential adsorption of residual products within the pores and/or minor re-arrangement or collapse of the network structure resulting from treatment in an acidic environment during repeated cycles. The FT-IR spectrum of the recovered catalyst demonstrated no significant change when compared to that of

the fresh catalyst. This observation confirms the stability and retention of almost all functional groups in the recycled catalyst after 10 runs (Fig. S24 and S25†). According to the CHNS analysis of the recycled catalyst, the loading amounts of imidazolium and HSO_4^- were 0.71 and 0.41 mmol g⁻¹, respectively (Table S4†). Additionally, the loading of the hydrogen sulfate anion after 10 cycles of reaction was assessed using the back titration method, giving a value of 0.43 mmol g⁻¹, which is slightly lower than that of the fresh catalyst. Hence, the slight decrease in catalyst activity observed in successive runs may be related to the minor reduction in the acid loading of the catalyst. Furthermore, VSM analysis of the recycled catalyst (Fig. S26 and S27†) revealed a magnetic saturation value of approximately 10 amu g⁻¹, which continues to provide a robust and adequate response to the separation of the catalyst from the reaction medium using an external magnet, even after 10 cycles. The obtained graph demonstrates reversibility, indicating that the recycled catalyst retains superparamagnetic properties. The slight reduction in magnetic saturation of the recycled catalyst compared to that of the fresh catalyst may be associated with the trace digestion of selected bare iron oxides within the catalyst structure due to exposure to the acidic environment in successive cycles. Finally, the TEM image of the recovered catalyst indicated that the uniform distribution of a core-shell structure and the total network structure of the catalyst remain intact even after repeated reaction runs (Fig. 6).

Finally, we proposed a reaction mechanism for the esterification reaction using catalyst 5, drawing upon the previously reported studies.^{45,46} According to the proposed mechanism illustrated in Scheme 2, initially, the acidic part of catalyst 5 initially functions as a proton donor to the carboxylic acid group, thereby starting the reaction pathway. Following the isomerization of the protonated acid, it becomes susceptible to a nucleophilic attack by the alcohol. Then, through a hydrogen transfer process, removal of water occurs, and the catalyst is regenerated *via* proton abstraction, ultimately resulting in the formation of the desired ester.

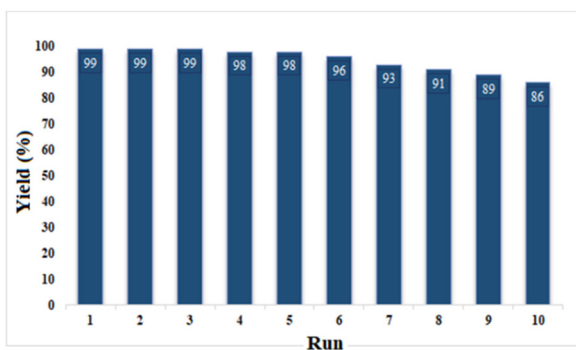


Fig. 5 Recovery of the $Fe_3O_4@SiO_2-S-xIm^+HSO_4^-$ catalyst in the direct esterification of 1-octanol with acetic acid.

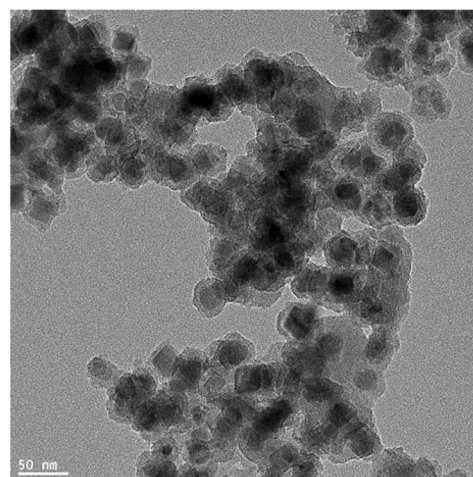
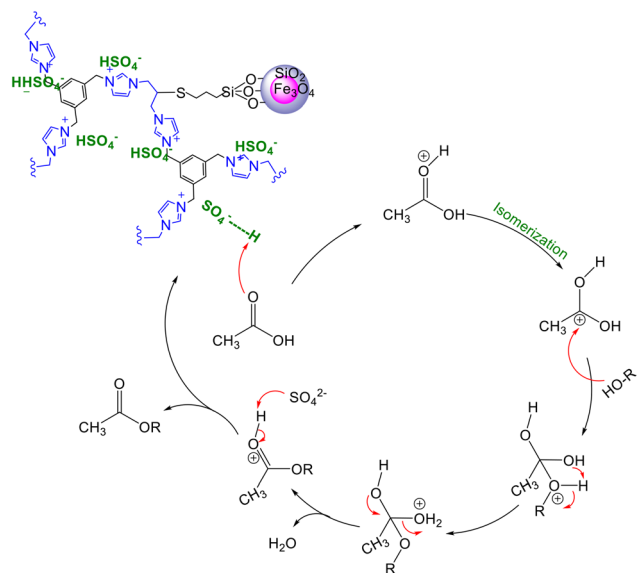


Fig. 6 TEM image of the recovered $Fe_3O_4@SiO_2-S-xIm^+HSO_4^-$ catalyst.



Scheme 2 Proposed mechanism for the direct esterification reaction of acetic acid and alcohols using Fe₃O₄@SiO₂-S-xIm⁺HSO₄⁻.

Conclusions

In summary, we have developed a novel hybrid organic-inorganic magnetic ionic network nanoparticle (MINN) comprising silica-coated iron oxide nanoparticles as seeds and a 3D imidazolium-based PIL as an organic linker. The prepared material was presented as a novel solid support with many combined features to immobilize acidic functional groups *via* a simple ion exchange process. The catalyst developed in this way exhibited outstanding catalytic activity, selectivity, durability and recoverability in the direct esterification reaction of primary and secondary benzylic, aliphatic and cyclic alcohols with acetic acid under solvent-free reaction conditions. The present catalyst system offers several advantages, including high efficiency, an excellent substrate scope, very low catalyst dosage (0.1 mol%), a high TON, and the convenience of separation from the reaction mixture using a magnetic bar. The catalyst was easily separated from the reaction mixture and reused in the esterification of 1-octanol with acetic acid up to 10 cycles with no significant loss of activity. We speculate that the pronounced reactivity, selectivity, and reusability of the developed catalyst could be primarily ascribed to the excellent distribution of highly active acidic catalytic sites across the well-designed three-dimensional PIL support, which forms a uniformly dispersed hydrophilic-hydrophobic balanced ionic-acidic nanoreactor. This configuration and matrix composition may facilitate the efficient diffusion of starting materials into the nanoscale spaces of the catalyst network, where the active sites are situated. Additionally, this arrangement may enable the rapid expulsion of water from the vicinity of the active sites, thereby contributing to a high-performance and durable catalyst system in the esterification reaction. In this context, our precise control experiments demonstrated that while the

support does not directly interfere with the reaction process, it plays a crucial role in enhancing the reaction yield, potentially through the aforementioned pathway. Overall, the material presented in this study exhibits several noteworthy characteristics, including a three-dimensional network structure, high ionic density, elevated thermal decomposition temperature, appropriate surface area, significant ionic liquid content, flexibility, excellent dispersibility in various media, and ease of recovery through magnetic separation. These attributes make it a promising candidate not only for catalytic applications but also for various other fields, such as separation technologies and electrochemistry. Further investigations into the potential applications of this material are currently being conducted by our research group.

Author contributions

M. F.: methodology, investigation, data curation, formal analysis, and writing – original draft. This research work is part of Maryam Faraji's MSc Dissertation at IASBS. F. M.: advising and writing – review & editing. B. K.: initial idea, conceptualization, supervision, data curation, and writing – review & final editing. H. V.: analysis.

Conflicts of interest

There are no conflicts to declare.

Data availability

All data and materials are included in the manuscript and its ESI.†

Acknowledgements

The authors thank the Institute for Advanced Studies in Basic Science (IASBS) (100/151/12882) Research Council for supporting this work. BK particularly appreciates the Alexander von Humboldt-Foundation for the donation of the prestigious Georg-Förster award (award no. ref. 3.4-1116632-IRN-GFPR) and the Iran National Science Foundation (INSF) through an international chair (INSF-Chair-4039182) for supporting this work.

References

- 1 Z. Lei, C. Dai, J. Hallett and M. Shiflett, *Chem. Rev.*, 2024, **124**, 7533–7535.
- 2 Q. Li, F. Yan and J. Texter, *Chem. Rev.*, 2024, **124**, 3813–3931.
- 3 A. S. Amarasekara, *Chem. Rev.*, 2016, **116**, 6133–6183.
- 4 F. Giacalone and M. Gruttadauria, *ChemCatChem*, 2016, **8**, 664–684.

- 5 A. Bohre, A. Modak, V. Chourasia, P. R. Jadhao, K. Sharma and K. K. Pant, *Chem. Eng. J.*, 2022, **450**, 138032.
- 6 B. Karimi and D. Enders, *Org. Lett.*, 2006, **8**, 1237–1240.
- 7 B. Karimi, M. Tavakolian, M. Akbari and F. Mansouri, *ChemCatChem*, 2018, **10**, 3173–3205.
- 8 M. Zhu and Y. Yang, *Green Chem.*, 2024, **26**, 5022–5102.
- 9 S. Y. Zhang, Q. Zhuang, M. Zhang, H. Wang, Z. Gao, J. K. Sun and J. Yuan, *Chem. Soc. Rev.*, 2020, **49**, 1726–1755.
- 10 B. Karimi, M. R. Marefat, M. Hasannia, P. F. Akhavan, F. Mansouri, Z. Artelli, F. Mohammadi and H. Vali, *ChemCatChem*, 2016, **8**, 2508–2515.
- 11 B. Karimi, Z. Artelli, F. Mohammadi, F. Mansouri, M. Hasannia, M. R. Marefat, H. Vali, P. Mastrorilli and S. Todisco, *ChemistrySelect*, 2019, **4**, 347–356.
- 12 R. Zhao, T. Han, D. Sun, L. Huang, F. Liang and Z. Liu, *Langmuir*, 2019, **35**, 11435–11442.
- 13 M. A. Neouze, M. Kronstein and F. Tielens, *Chem. Commun.*, 2014, **50**, 10929–10936.
- 14 P. Zhang, Z. A. Qiao, X. Jiang, G. M. Veith and S. Dai, *Nano Lett.*, 2015, **15**, 823–828.
- 15 M. Litschauer and M. A. Neouze, *J. Mater. Chem.*, 2008, **18**, 640–646.
- 16 M. A. Neouze, M. Litschauer, M. Puchberger and H. Peterlik, *Langmuir*, 2011, **27**, 4110–4116.
- 17 L. H. Reddy, J. L. Arias, J. Nicolas and P. Cuvreur, *Chem. Rev.*, 2012, **112**, 5818–5878.
- 18 V. Polshettiwar, R. Luque, A. Fihri, H. Zhu, M. Bouhrara and J. M. Basset, *Chem. Rev.*, 2011, **111**, 3036–3075.
- 19 B. Karimi, F. Mansouri and H. M. Mirzaei, *ChemCatChem*, 2015, **7**, 1736–1789.
- 20 A. Pourjavadi, S. H. Hosseini, M. Doulabi, S. M. Fakoorpoor and F. Seidi, *ACS Catal.*, 2012, **2**, 1259–1266.
- 21 B. Karimi, F. Mansouri and H. Vali, *Green Chem.*, 2014, **16**, 2587–2596.
- 22 M. Gholinejad, F. Zareh, H. Sheibani, C. Nájera and M. Yus, *J. Mol. Liq.*, 2022, **367**, 120395.
- 23 S. Sadjadi, *J. Mol. Liq.*, 2021, **323**, 114994.
- 24 B. Karimi, M. Tavakolian, F. Mansouri and H. Vali, *ACS Sustainable Chem. Eng.*, 2018, **7**, 3811–3823.
- 25 J. Piotrowska, C. Jordan, K. Stagel, M. Annerl, J. Willner, A. Limbeck, M. Harasek and K. Bica-Schröder, *React. Chem. Eng.*, 2025, **10**, 360–370.
- 26 M. Gabrič, F. M. Harth, B. Hočevár, S. Gyergyek, B. Likozar and M. Grilc, *Green Chem.*, 2025, **27**, 3640–3645.
- 27 Y. Tang, J. Chen, X. Zhu and X. Lu, *Surf. Interfaces*, 2025, **72**, 107020.
- 28 H. M. Levy, T. H. S. Rodrigues, T. L. de Albuquerque, H. B. Sant'Ana, F. X. Feitosa and M. V. P. Rocha, *Renewable Energy*, 2025, **243**, 122452.
- 29 C. J. Yue, X. Sun, H. Xiao and X. Y. Jin, *ACS Sustainable Chem. Eng.*, 2025, **13**, 8003–8012.
- 30 J. Chen, J. Wu, T. Veldhuis, F. Picchioni, P. Raffa and C. E. Koning, *ACS Sustainable Chem. Eng.*, 2025, **13**, 559–570.
- 31 P. Zhang, Y. Sun, Q. Zhang, Y. Guo and D. Song, *Fuel*, 2018, **228**, 175–186.
- 32 K. Suwannakarn, E. Lotero and J. G. Goodwin, *Ind. Eng. Chem. Res.*, 2007, **46**, 7050–7056.
- 33 T. Akiyama, *Chem. Rev.*, 2007, **107**, 5744–5758.
- 34 X. Ma, F. Liu, Y. Helian, C. Li, Z. Wu, H. Li, H. Chu, Y. Wang, Y. Wang, W. Lu and M. Guo, *Energy Convers. Manage.*, 2021, **229**, 113760.
- 35 L. He, S. Qin, T. Chang, Y. Sun and X. Gao, *Catal. Sci. Technol.*, 2013, **3**, 1102–1107.
- 36 B. Karimi, B. Ghaffari and H. Vali, *J. Colloid Interface Sci.*, 2021, **589**, 474–485.
- 37 T. Karimpour, E. Safaei, F. Mansouri and B. Karimi, *Appl. Surf. Sci.*, 2025, **682**, 161616.
- 38 B. Karimi and M. Vafaezadeh, *Chem. Commun.*, 2012, **48**, 3327–3329.
- 39 S. Yin, J. Sun, B. Liu and Z. Zhang, *J. Mater. Chem. A*, 2015, **3**, 4992–4999.
- 40 B. Karimi, H. M. Mirzaei and A. Mobaraki, *Catal. Sci. Technol.*, 2012, **2**, 828–834.
- 41 J. C. Manayil, C. V. Inocencio, A. F. Lee and K. Wilson, *Green Chem.*, 2016, **18**, 1387–1394.
- 42 J. Cao, B. Qi, J. Liu, Y. Shang, H. Liu, W. Wang, J. Lv, Z. Chen, H. Zhang and X. Zhou, *RSC Adv.*, 2016, **6**, 21612–21616.
- 43 T. Verheyen, M. Smet and W. M. De Borggraeve, *ChemistrySelect*, 2017, **2**, 9822–9828.
- 44 H. Baek, M. Minakawa, Y. M. Yamada, J. W. Han and Y. Uozumi, *Sci. Rep.*, 2016, **6**, 25925.
- 45 G. Jyoti, A. Keshav and J. Anandkumar, *Int. J. Chem. React. Eng.*, 2016, **14**, 571–578.
- 46 A. H. Fauzi and N. A. Amin, *Renewable Sustainable Energy Rev.*, 2012, **16**, 5770–5786.